

This is a repository copy of Determining aluminium co-ordination of kaolinitic clays before and after calcination with electron energy loss spectroscopy.

White Rose Research Online URL for this paper: <a href="https://eprints.whiterose.ac.uk/id/eprint/232927/">https://eprints.whiterose.ac.uk/id/eprint/232927/</a>

Version: Published Version

#### Article:

Marsh, A.T.M., Brown, A.P., Freeman, H.M. et al. (3 more authors) (2024) Determining aluminium co-ordination of kaolinitic clays before and after calcination with electron energy loss spectroscopy. Applied Clay Science, 255. 107402. ISSN: 0169-1317

https://doi.org/10.1016/j.clay.2024.107402

# Reuse

This article is distributed under the terms of the Creative Commons Attribution (CC BY) licence. This licence allows you to distribute, remix, tweak, and build upon the work, even commercially, as long as you credit the authors for the original work. More information and the full terms of the licence here: https://creativecommons.org/licenses/

#### Takedown

If you consider content in White Rose Research Online to be in breach of UK law, please notify us by emailing eprints@whiterose.ac.uk including the URL of the record and the reason for the withdrawal request.



ELSEVIER

Contents lists available at ScienceDirect

# **Applied Clay Science**

journal homepage: www.elsevier.com/locate/clay



# Research Paper



# Determining aluminium co-ordination of kaolinitic clays before and after calcination with electron energy loss spectroscopy

Alastair T.M. Marsh <sup>a,\*</sup>, Andy P. Brown <sup>b</sup>, Helen M. Freeman <sup>a</sup>, Brant Walkley <sup>c</sup>, Helen Pendlowski <sup>d</sup>, Susan A. Bernal <sup>a</sup>

- <sup>a</sup> School of Civil Engineering, University of Leeds, Leeds LS2 9JT, United Kingdom
- <sup>b</sup> School of Chemical and Process Engineering, University of Leeds, Leeds LS2 9JT, United Kingdom
- Department of Chemical and Biological Engineering, University of Sheffield, Sheffield S1 3JD, United Kingdom
- <sup>d</sup> The James Hutton Institute, Craigiebuckler, Aberdeen AB15 8QH, United Kingdom

#### ARTICLE INFO

# Keywords: Monochromated EELS Low dose TEM Kaolinite Metakaolin Calcined clays Solid State NMR

#### ABSTRACT

Developing a greater understanding of kaolinite dehydroxylation upon calcination is crucial for several industrial applications, including cements. Aluminium coordination in meta-kaolinite indicates the extent of its dehydroxylation and its potential chemical reactivity, and it is typically determined using <sup>27</sup>Al magic angle spinning (MAS) nuclear magnetic resonance (NMR) spectroscopy. This technique however presents limitations for Fe-rich materials, given the magnetic properties of Fe ions and minerals containing Fe. In this study, the effect of calcination on Al coordination was assessed in a low-Fe clay used as a reference system, and a Fe-rich clay. Al coordination in the low-Fe clay was quantified via <sup>27</sup>Al MAS NMR spectra deconvolution, using data collected at 9.4 T and 11.7 T. Energy dispersive X-ray spectroscopy (EDX) maps and electron energy loss spectroscopy (EELS) measurements were carried out in a scanning transmission electron microscope (STEM) on both clays. Al K-edge EEL spectra showed distinguishable 4/5-fold Al and 6-fold Al sites in both clay types. Differences in line-profile indicated a higher proportion of 4/5-fold Al in kaolinite in the Fe-rich clay compared to the low-Fe clay. Conversely, the Fe-rich clay contained a lower proportion of 4/5-fold Al in meta-kaolinite after calcination, relative to the low-Fe clay. These differences are consistent with the greater structural disorder of the metakaolinite identified in the Fe-rich clay by X-ray diffraction and the geological origins of both clays. Overall, this study demonstrates the potential of EELS to provide information about Al coordination for individual kaolinite and meta-kaolinite particles.

# 1. Introduction

Kaolinite is a di-octahedral 1:1 clay mineral, with each 1:1 layer consisting of an octahedral sheet of alumina bonded via shared oxygen ions to a tetrahedral sheet of silica. It has the chemical composition Al<sub>2</sub>Si<sub>2</sub>O<sub>5</sub>(OH)<sub>4</sub>, resulting in a net layer charge of zero (Brigatti et al., 2006). Calcining kaolinite in air at an optimal temperature range (typically within 600–800 °C) results in formation of meta-kaolinite – a highly disordered form of kaolinite that is X-ray amorphous and highly reactive (relative to its un-calcined form) (Heller-Kallai, 2006). Loss of hydroxyl groups distorts the Al octahedra, which causes significant structural disorder in the octahedral sheet; in turn, this results in distortion of the tetrahedral sheet as Si tetrahedra rotate to adapt to the new configuration (Bergaya et al., 1996; White et al., 2010). As a result,

there is buckling of individual 1:1 layers, and a subsequent loss of longterm order in all crystallographic axes. Hereafter "meta-kaolinite" will be used to describe the disordered form of kaolinite, and "metakaolini" will be used to describe a clay which contains meta-kaolinite alongside associated minerals. Because of well-established limitations and ambiguities around the use of "crystallinity" to describe clay minerals, the term "structural order" will be used instead (Guggenheim et al., 2002).

A major emerging application of calcined clays is in cementitious materials, including as a substitute for Portland cement (Scrivener et al., 2018) and as a precursor for alkali-activated cements (Khalifa et al., 2020). Much investigation has gone into understanding the links between clay mineralogy, calcination conditions, and the chemical reactivity of calcined clays in cementitious systems, a process that is somewhat complicated by the variety in mineralogy of clay-based

E-mail address: a.marsh@leeds.ac.uk (A.T.M. Marsh).

<sup>\*</sup> Corresponding author.

resources (Alujas Diaz et al., 2022). There is debate regarding the exact role and influence that Al coordination has on a calcined clay's chemical reactivity. The fraction of 5-fold co-ordination Al has been proposed as an indicator of reactivity for meta-kaolinite (Rocha and Klinowski, 1990a), while subsequent studies argue against this (Fabbri et al., 2013; Kuenzel et al., 2013).

Magic angle spinning nuclear magnetic resonance (MAS NMR) spectroscopy is typically used to explore changes in Al coordination after calcination (Walkley and Provis, 2019). Using appropriate models that account for quadrupolar broadening, e.g. the Czjzek model (d'Espinose de Lacaillerie et al., 2008), it is possible to deconvolute <sup>27</sup>Al MAS NMR spectra and hence obtain quantitative measurements of the proportions of sites in each coordination state (Massiot et al., 1995). When applied to as-received kaolinite, there is a general consensus that nearly all Al sites are in 6-fold coordination. If calcined at high temperatures sufficient to cause re-crystallisation (typically above 900 °C), nearly all Al sites are in 4-fold co-ordination. In meta-kaolinite, <sup>27</sup>Al MAS NMR spectra exhibit three distinct resonances, with a distribution of Al sites in broadly similar proportions - typically assigned to 4-fold, 5-fold and 6-fold coordination states (Massiot et al., 1995; Rocha, 1999). However, the assignment of the mid-range resonance as 5-fold Al is contested - an alternative interpretation is 4-fold Al coordination in a highly disordered local environment, wherein the disorder causes a substantial deviation in chemical shift from the expected range for 4-fold Al in aluminosilicates (MacKenzie et al., 1985; McManus et al., 2001; Izadifar et al., 2020). There is further debate around 6-fold Al in meta-kaolinite. Studies consistently report a substantial resonance associated with 6fold Al in meta-kaolinite's <sup>27</sup>Al MAS NMR spectrum (Rocha and Klinowski, 1990a; Massiot et al., 1995; Rocha, 1999), yet structural models developed from neutron scattering yield no 6-fold Al remaining at all (White et al., 2010). Given that a detailed scientific understanding of meta-kaolinite's structure and the dehydroxylation process itself is not yet complete, additional characterisation techniques have value in bringing new perspectives to these fundamental questions.

A drawback of MAS NMR is that the presence of species that exhibit paramagnetism in substantial quantities (e.g. Fe, Mn), and mineral particles that may be ferro/ferrimagnetic (e.g. Fe<sub>3</sub>O<sub>4</sub>, Fe<sub>2</sub>O<sub>3</sub>), significantly degrades the spectral quality (Kirkpatrick et al., 1985). These phenomena present an obstacle to studying clays that also contain Febased minerals (typically goethite and hematite). Fe-rich clays are abundant in regions of the world projected to have a high demand for construction in the coming years (e.g. the Indian subcontinent, West Africa). The kaolinite present in lateritic clays can vary with regard to its particle size, degree of structural ordering and extent of octahedral Fe<sup>3+</sup> substitution, depending on its position in the weathering profile (Beauvais, 1999). There is an established trend between the amount of Fe substitution in a kaolinite specimen, and its extent of structural disorder (Mestdagh et al., 1980; Brindley et al., 1986). There is increasing research interest in using Fe-rich clays for cementitious materials' precursors, due to the relatively low dehydroxylation temperatures of disordered kaolinites (Kaze et al., 2017), and the potential for Fe to participate in binder phase formation (Kaze et al., 2021). Hydrochloric acid treatments have been used to remove Fe oxide and (hydr)oxide minerals from clay (Schroeder and Pruett, 1996); whilst such treatments have been adapted to avoid altering the kaolinite structure as far as possible, it is well-established that acid treatments tend to result in preferential dissolution of Al<sup>3+</sup> (Komadel and Madejová, 2006).

Electron Energy Loss Spectroscopy (EELS) within a Transmission Electron Microscope (TEM) offers a potential alternative method for measuring Al co-ordination, and has not been used to study kaolinite calcination so far. The shape or near-edge profile of the Al *K*-edge acquired by TEM-EELS (or in this case Scanning (S) TEM-EELS) can be used to identify Al coordination states for different aluminosilicate minerals (Hansen et al., 1994) and glasses (Liao et al., 2020). X-ray near-edge absorption spectra (XANES) show differences in the Al *K*-edge profile for different Al coordination states (Li et al., 1995; Ildefonse et al.,

1998). XANES studies have investigated the coordination state of kaolinite (Li et al., 1995; Ildefonse et al., 1998), and meta-kaolinite (White et al., 2011; Andrini et al., 2016). However, XANES has the practical disadvantage of largely being restricted to synchrotrons. In contrast, TEM-EELS is a laboratory-based microscopy technique, and can provide spectral information at the individual particle level (Egerton, 2008). In addition EELS does not suffer the limitations arising from high Fe concentrations that MAS NMR does. Therefore, the use of EELS for investigating the structural changes induced by calcination in Fe-rich clays offers added value beyond what XANES and  $^{27}\mathrm{Al}$  MAS NMR can provide. A challenge of using EELS is the beam-sensitivity of kaolinite samples; high energy electrons can cause radiolytic damage leading to the loss of structural hydroxyl groups and even oxygen, giving rise to a change in corresponding metal co-ordination (Garvie et al., 2004; Pan et al., 2010). There is therefore a need to use EELS measurement conditions at sufficiently low electron fluence to avoid radiolysis-induced sample damage, whilst still achieving the desired spectral resolution and signal to noise to measure metal co-ordination (Freeman et al.,

This study evaluated the feasibility of using STEM-EELS to measure coordination changes of Al in kaolinite upon calcination; and its potential applicability to determine Al coordination changes in Fe-rich kaolinitic clays. The approach of this study was to use <sup>27</sup>Al MAS NMR measurements on a low-Fe clay to benchmark the use of EELS for this mineral system, and then to use STEM-EELS on an Fe-rich clay to assess the change in kaolinite Al co-ordination induced by calcination.

#### 2. Materials and methods

## 2.1. Clays evaluated

Two kaolinitic clays were selected for this study – one low-Fe clay (1.1 wt%  $Fe_2O_3$ ), and one Fe-rich clay (24.4 wt%  $Fe_2O_3$ ) (Table 1). The chemical oxide composition of the clays was measured by X-ray fluorescence (XRF) spectroscopy (Table 1), using a Rigaku ZSX Primus II, with the fused bead preparation method and a loss on ignition (LOI) heating step carried out at 900  $^{\circ}\text{C}$  for 2 h.

The low-Fe clay was a purified china clay (Imerys PolwhiteE). This is a commercial kaolin product from the well-known kaolinized granite deposit in Cornwall, U.K. (Imerys Imerys Kaolin, 2019), in which muscovite is commonly found alongside remaining K-feldspar and quartz as associated minerals (Exley, 1976; Psyrillos et al., 1998). The quantities of each mineral phase were calculated independently by quantitative XRD analysis using the Rietveld refinement method (Ufer and Raven, 2017), as 73.5 wt% kaolinite, 17.9 wt% muscovite, 5.6 wt% K-feldspar and 3.0 wt% quartz.

The Fe-rich clay was sourced from the lithomargic layer of the Interbasaltic Formation in Co. Antrim, Northern Ireland, U.K. (McIntosh et al., 2015). In this formation, kaolinite is formed via neogenesis from the weathering of silicates (inc. feldspar, pyroxene, olivine) found in basalt (Hill et al., 2000). The quantities of each mineral phase were calculated independently by quantitative XRD analysis using the relative intensity ratio method (Omotoso et al., 2006; Butler and Hillier, 2021), as 62.7 wt% kaolinite, 29.0 wt% goethite, 2.7 wt% hematite, 2.6 wt% magnetite, 1.6 wt% gibbsite, and 0.3 wt% anatase.

The low-Fe clay was evaluated as a reference system on which both  $^{27}$ Al MAS NMR and STEM-EELS measurements were carried out. Only STEM-EELS was applied to the Fe-rich clay, for which  $^{27}$ Al MAS NMR measurements would yield data in which  $^{27}$ Al signals would typically be too broad to be informative. Changes identified by STEM-EELS are validated against  $^{27}$ Al MAS NMR measurements for the low-Fe clay, and STEM-EELS then used to investigate the Fe-rich clay.

# 2.2. Calcination process

Both clays were calcined by heating at 750 °C for 1 h in air, hot-

Table 1
Chemical oxide composition of the two clays in wt%.

	$SiO_2$	$Al_2O_3$	$Fe_2O_3$	K <sub>2</sub> O	$TiO_2$	MgO	CaO	$P_2O_5$	Na <sub>2</sub> O	MnO	$Cr_2O_3$	Others (<0.1 wt%)	LOI
Low-Fe clay	49.05	34.80	1.12	3.25	_	0.32	0.05	0.10	0.21	-	-	0.18	10.92
Fe-rich clay	29.48	25.89	24.36	0.06	3.14	0.65	0.49	0.24	-	0.16	0.14	0.30	14.89

loaded into a Carbolite 1100 AAF static laboratory furnace. A calcination temperature of 750  $^{\circ}\text{C}$  was selected, as no further mass loss due to dehydroxylation was observed above this temperature from either clays' TG curves. A mass of 10 g of clay was loaded in a shallow porcelain crucible.

#### 2.3. Characterisation methods

Powder X-ray diffraction (XRD) was used to identify the mineral phases present in the as-received and calcined clays, and also to assess the extent of structural disorder upon dehydroxylation caused by calcination. Data were collected using a Panalytical Empyrean diffractometer (45 kV, 40 mA) in Bragg-Brentano geometry, with a two-axis goniometer geometry and a Cu K $\alpha$  X-radiation source ( $\lambda=1.5406$  Å). Incident beam optics of a soller slit 0.03 rad, divergence slit ½ deg. rad (0.5 mm) and diffracted beam optics of soller slit 0.04 rad, anti-scatter slit ½ deg. rad (0.5 mm) were used, with no monochromator. Measurement conditions were:  $2\theta$  range of 4– $70^{\circ}$ , a step size of  $0.0131^{\circ}2\theta$ , a time per step of 100 s, and a spinning speed of 30 rotations/min. Powder diffraction files (PDFs) from the International Centre for Diffraction Data (ICDD) PDF-4+ 2023 database were used to identify mineral phases.

Thermogravimetry was used to confirm that full dehydroxylation of kaolinite had taken place during calcination. A Netzsch STA 449 F5 was used, with a heating range between 30 and 1000  $^{\circ}\text{C}$ , and a heating rate of 10  $^{\circ}\text{C/min}$ , in an  $N_2$  gas atmosphere with an  $N_2$  gas flow rate of 60 mL/min. A sample mass of 20 mg was used in alumina crucibles.

<sup>27</sup>Al MAS NMR spectroscopy was used to measure the changes in Al coordination in the low-Fe clay after calcination. A Bruker Avance III HD (400 MHz, magnetic field 9.4 T) was used at an operating frequency of 104.26 MHz. Alumina rotors of 2.5 mm diameter were used, with a spinning speed of  $\nu_R = 20$  kHz and an excitation pulse of 0.23 μs. 4096 scans were collected for each spectrum. Yttrium Aluminium Garnet (YAG) was used as a secondary standard with the hexacoordinated site referenced to 0.7 ppm. Additional <sup>27</sup>Al MAS NMR spectra were collected with a different Bruker Avance III HD (500 MHz, magnetic field 11.7 T), at an operating frequency of 130.32 MHz. ZrO<sub>2</sub> rotors of 4 mm diameter were used, with a spinning speed of  $\nu_R = 12.5$  kHz, and an excitation pulse of 1.7 μs. Topspin 3.6.4 (Bruker) was used for initial phase adjustment and line broadening. Spectra were presented after constant sum normalisation (Giraudeau et al., 2014).

Deconvolution of <sup>27</sup>Al MAS NMR spectra was carried out in dmfit software (Massiot et al., 2002). Five peaks were fitted for the low-Fe clay's spectrum: a 6-fold Al resonance representing octahedral Al sites in kaolinite, a 6-fold Al resonance representing octahedral Al sites in a muscovite impurity, a minor 6-fold Al resonance as an artefact of quadrupolar interactions, a 4-fold Al resonance corresponding to tetrahedral Al sites in a muscovite impurity, and a 4-fold Al resonance corresponding to a K-feldspar impurity. Three peaks were fitted for the calcined low-Fe clay's spectrum, representing the main resonances found in meta-kaolinite: 6-fold Al, 4-fold Al, and a third resonance which will hereafter be referred to as the "mid-range Al resonance", given the true coordination state of this resonance is still under debate. Full attributions of the individual peaks fitted are described in Section 3.1. Quadrupolar coupling constants  $(C_q)$  were varied to obtain the best overall fit, broadly within the ranges established by previous studies for the main resonances (Table 2). Using similar Cq values for the three main resonances in meta-kaolinite is appropriate, as a broadly similar extent of quadrupolar coupling across the three main resonances has been established for meta-kaolinite and similar amorphous aluminosilicates

**Table 2**Quadrupolar coupling constant values (MHz) used in previous <sup>27</sup>Al MAS NMR studies for the main resonances in kaolinite and meta-kaolinite.

Kaolinite		Meta-kao	linite	Reference	
6-fold site 1	6-fold site 2	6-fold	5-fold / mid- range	4-fold	
3.4	3.0	_	_	_	(Paris, 2014)
3.4	-	-	-	-	(Newman et al., 1994)
3.36	2.88	-	-	-	(Hayashi et al., 1992)
_	_	_	5.0	5.4	(Rocha, 1999)
-	-	3.0-4.6	5.0	5.0-5.4	(Sankar et al., 2019)
-	-	3.5-4.6	4.0–5.0	3.4–5.0	(Izadifar et al., 2020)

(McManus et al., 2001). Resonance intensity and full-width half maximum values were then iterated in order to achieve the best agreement with the overall measured signal, whilst maintaining an acceptable fit with the individual resonance lineshapes. Spectra collected from two different magnetic fields ( $B_0 = 9.4 \text{ T}$  and 11.7 T) were used in order to provide confidence to fitting, as done by Sankar et al. (2019). Fitting parameters are provided in Table S2 in the Supplementary Information. The uncertainty in quantification within each spectrum was estimated to be equivalent to the % signal to noise ratio in each respective measured spectrum.

Scanning transmission electron microscopy (STEM) was used alongside energy dispersive spectroscopy (EDX) to identify individual mineral particles on the basis of size, morphology and composition. EELS was used to measure the coordination states of Al for particles of interest. A Thermofisher Titan<sup>3</sup> Themis G2 STEM was used with a monochromator, a Thermofisher Super-X EDX detector, a Gatan One-View camera, and a Dual EELS Gatan Quantum 965 ER energy filter. Samples were prepared by dispersing in ethanol, sonicating and then drop-casting onto holey carbon film (EM resolutions).

The standard Thermofisher double-tilt sample holder and regular vacuum conditions were used. In TEM mode, the magnification was limited to  $<\!185$  kX maximum with an accelerating voltage of 300 kV and a probe current of 200 pA. Fig. 1 shows resolution of unaltered basal planes of kaolinite in an image acquired under these conditions of a stack of kaolinite in the as-received low-Fe clay. The kaolinite (001) lattice spacing was measured as  $\sim\!0.71$  nm, considered to match well with a value for fully hydrated kaolinite of 0.74 nm obtained by X-ray diffraction data (Bish and Von Dreele, 1989). No significant plane warping or breakdown was observed, and this level of beam intensity was therefore assumed to be on or below the threshold for significant damage to kaolinite in the microscope.

For STEM-EELS measurements, a monochromator energy spread of ca. 0.4 eV was used in order to achieve satisfactory energy resolution at the Al K-edge. Spectra were acquired by continuously scanning a monochromated,  $\sim 350$  pA focussed probe (of 0.14 nm diameter) across individual mineral plates imaged at < 180 kX with an electron energy loss collection semi-angle of 29 mrad and a convergence semi-angle of 10 mrad (as detailed previously in Freeman et al. (2019). Any orientation dependence at the Al K-edge was minimised by consistently acquiring spectra at a large collection angle (i.e., > 10 times the characteristic scattering angle for inelastic scattering at 1560 eV energy loss) from kaolinite/meta-kaolinite plates lying flat on the carbon support film, as

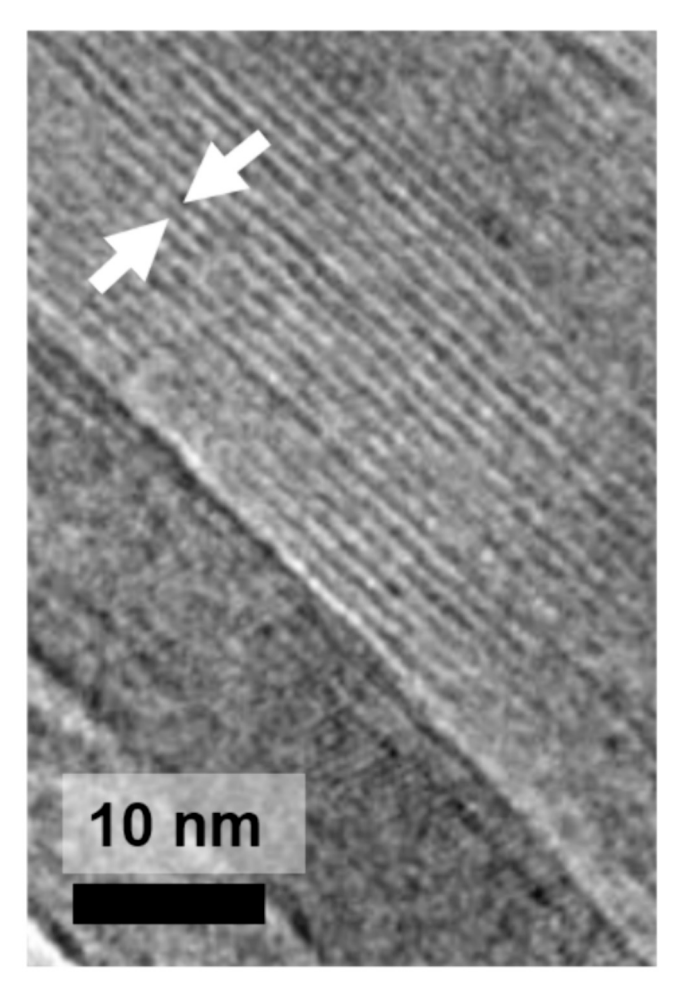


**Fig. 1.** 0.7 nm lattice fringe spacing for a stack of kaolinite in the as-received low-Fe clay. Arrows indicate an individual kaolinite platelet, viewed perpendicular to the c-axis.

these tend to have the c-axis normal to the film. The dwell time of the electron probe was limited to  $\sim 1~\mu s$ , in order to ensure minimal damage per dwell point. Spectra were collected for 30 s continuous scanning and

then background subtracted (power law) in 'Gatan Microscopy Suite' software (v 3.0.1). In order to reduce spectral noise, a 40 point moving average was applied to all spectra before displaying the final results and the 'typical' spectrum of at least three representative spectra presented.

STEM-EDX spectroscopy and elemental mapping was carried out using the FEI Super-X detector and Velox software, under the same probe and acquisition conditions as for STEM-EELS. EDX spectra were used in-situ to distinguish kaolinite particles from impurity minerals on the basis of their chemical composition, a similar approach to that used in previous studies (Day-Stirrat et al., 2017; Woodward et al., 2018). For example, muscovite in the low-Fe clay was distinguished by its potassium content, and gibbsite in the Fe-rich clay by its lack of silicon. Thus, EELS measurements were made solely on kaolinite or meta-kaolinite particles.

#### 3. Results and discussion

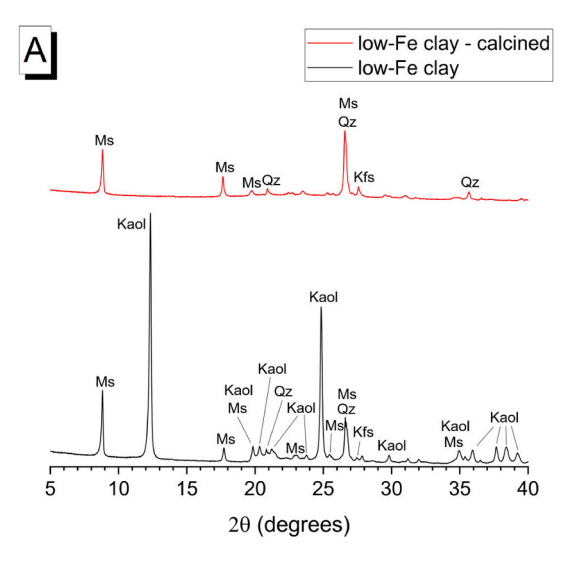
#### 3.1. Characterisation of low-Fe clays

Powder XRD patterns of the low-Fe kaolinitic clay show the disappearance of kaolinite (powder diffraction file (PDF) # 01–079-1570) reflections after calcination (Fig. 2a). The kaolinite 001 reflection at 12.3°20 corresponds to a basal spacing of 7.2 Å. In contrast, the reflections of quartz (PDF# 00–046-1045), muscovite (PDF # 01–084-1304) and K-feldspar (PDF# 00–019-0932) are still clearly visible. In the thermogravimetric (TG) curves (Fig. 2b), the mass loss associated with the dehydroxylation of kaolinite is clearly visible for the as-received clay in the range of 400–700 °C. The kaolinite content of the low-Fe clay was confirmed to be ~70 wt%, by comparing the mass loss over the temperature range characteristic of dehydroxylation against the ideal mass loss of dehydroxylation for pure kaolinite (14 wt%) (Mackenzie and Caillère, 1975) (Eq. 1). After calcination, negligible mass loss was observed over this temperature range, indicating that dehydroxylation was complete or near-complete when calcined for 1 h at 750 °C.

Equation 1: Estimation of kaolinite content in a material by thermogravimetry (Snellings et al., 2022).

$$\textit{Kaolinite content} = \frac{100 \times \left(\textit{Mass}_{\textit{pre}-\textit{dehydroxylation}} - \textit{Mass}_{\textit{post}-\textit{dehydroxylation}}\right)}{\textit{Mass}_{\textit{dry}} \times 14} \tag{1}$$

In the  $^{27}$ Al MAS NMR spectrum for the as-received low-Fe clay, the main resonance exhibited an observed chemical shift centred at  $\delta_{\text{obs}}$  =



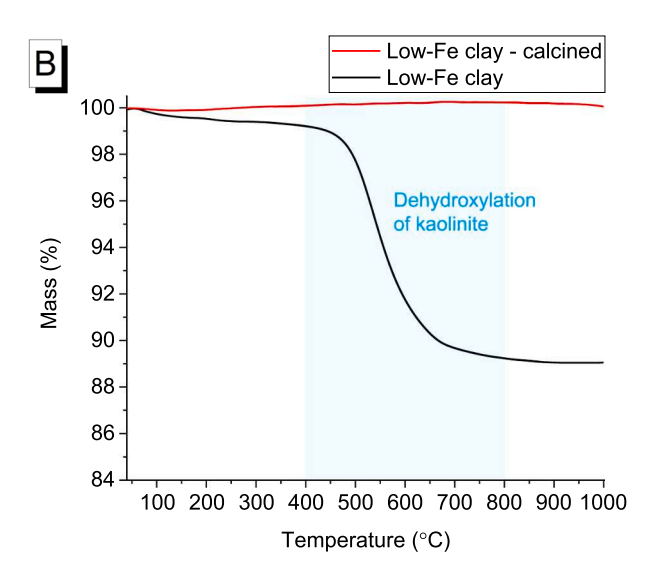


Fig. 2. a) XRD patterns and b) TG curves of the low-Fe clay before (black) and after (red) calcination. Kaol = kaolinite; Kfs = K-feldspar; Ms. = muscovite; Qz = quartz. (For interpretation of the references to colour in this figure legend, the reader is referred to the web version of this article.)

0.5 ppm (Fig. 3), independently of the magnetic field used. The majority of Al sites were therefore in 6-fold co-ordination, attributed to octahedral Al sites in kaolinite (Kinsey et al., 1985; Massiot et al., 1995) and a minor contribution from octahedral Al sites in the muscovite impurity (Kinsey et al., 1985; Lippmaa et al., 1986).

A shoulder at  $\delta_{\rm obs}=16.0$  ppm was observed in the spectrum acquired at  $B_0=9.4$  T, but not in the spectrum acquired at  $B_0=11.7$  T. The same phenomenon was observed by Zhou et al. (2009), who attributed this difference to the stronger influence of second-order quadrupolar interactions in the lineshape at lower field strengths. A weak resonance at  $\delta_{\rm obs}=69.0$  ppm was attributed to 4-fold Al in the muscovite impurity (Kinsey et al., 1985; Lippmaa et al., 1986). Another weak resonance at  $\delta_{\rm obs}=55.5$  ppm was attributed to 4-fold Al in the K-feldspar impurity (Xiao et al., 1995), although some contribution may also arise from Al substitutions in the tetrahedral sheet in kaolinite (Mantovani et al., 2009).

After calcination, the lineshape of the spectrum was much broader, consistent with the significant degree of structural disorder in metakaolinite. Multiple overlapping resonances in the spectrum acquired at  $B_0 = 9.4$  T (Fig. 3a) were observed at  $\delta_{obs} = 55.5$  ppm attributed to 4-fold Al,  $\delta_{\rm obs} = 24.0$  ppm attributed to the mid-range Al resonance and the shoulder at  $\delta_{\rm obs} = 9.0$  ppm attributed to 6-fold Al (Massiot et al., 1995). Minor contributions from the muscovite and K-feldspar impurities to the measured spectrum were expected to be similar to these minerals' resonances in the as-received clay's spectrum - from previous studies on heating muscovite (Mackenzie et al., 1987) and K-feldspar (Xiao et al., 1995), no significant changes to their Al coordination are considered likely after heating for 1 h at 750 °C. The three observed resonances were sharper and more clearly resolved in the spectrum acquired at  $B_0 =$ 11.7 T as compared to the spectrum acquired at  $B_0 = 9.4$  T, particularly for the mid-range and 4-fold Al resonances. Given the distorted nature of Al environments in meta-kaolinite, higher field strengths and spinning speeds typically give better resolution of the constituent resonances (Rocha, 1999; Sankar et al., 2019).

The quantitative results of the deconvolution of the  $^{27}$ Al MAS NMR spectra showed (Fig. 4) that in the low-Fe clay, the vast majority (>93%) of Al was in 6-fold coordination. Fittings and fitting parameters are shown in Fig. S1 and Table S2 respectively in the Supplementary Information. Good agreement was obtained between the values obtained from the spectra of both field strengths.

In the calcined low-Fe clay, Al was present in approximately equal

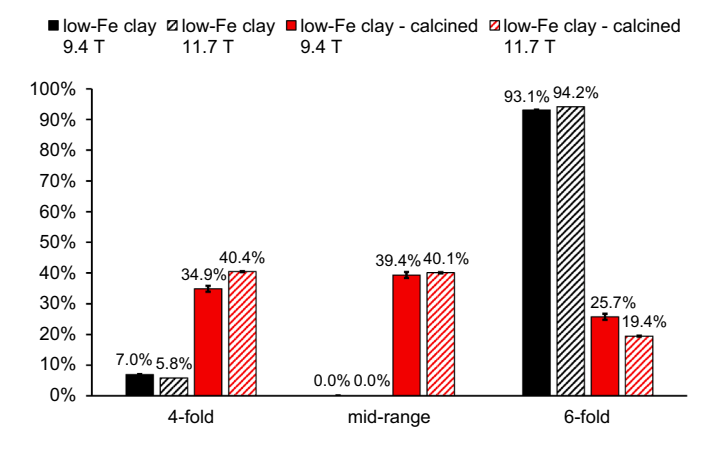


**Fig. 4.** Quantitative estimates of different Al coordination sites in the asreceived low-Fe clay and the calcined low-Fe clay respectively. Deconvolutions were carried out on  $^{27}$ Al MAS NMR spectra collected at 9.4 T and 11.7 T field strengths; the uncertainty in quantification within each spectrum, as shown in the error bars, was estimated from the signal to noise ratio of each measured spectrum.

proportions of 4-fold coordination (37.7%) and in the mid-range resonance (39.7%), with a smaller amount also present in 6-fold coordination (22.6%). These percentages correspond to average values from the two field strengths' datasets in Fig. 4, and the values lie within the range reported by previous studies (Table 3) (Lambert et al., 1989; Rocha and Klinowski, 1990b; Massiot et al., 1995; Sankar et al., 2019; Izadifar et al., 2020). Differences between sets of reported values can arise from a combination of several factors: <sup>27</sup>Al MAS NMR measurement parameters; the somewhat subjective nature of peak-fitting; and, most notably, differences in starting clays and calcination conditions (Massiot et al., 1995). Lambert et al. (1989) estimated the uncertainty in measuring the proportions of Al in different coordination states to be approximately 10%. The range of values reported by Sankar et al. (2019) for five industrially sourced metakaolin clays (Table 3) show that, even when multi-operator variation is eliminated, there is inherent variation between clays.

Dimensional changes induced by dehydroxylation are known to cause buckling of individual kaolinite layers (Gualtieri and Bellotto, 1998; White et al., 2010). Whilst these changes are substantial at the

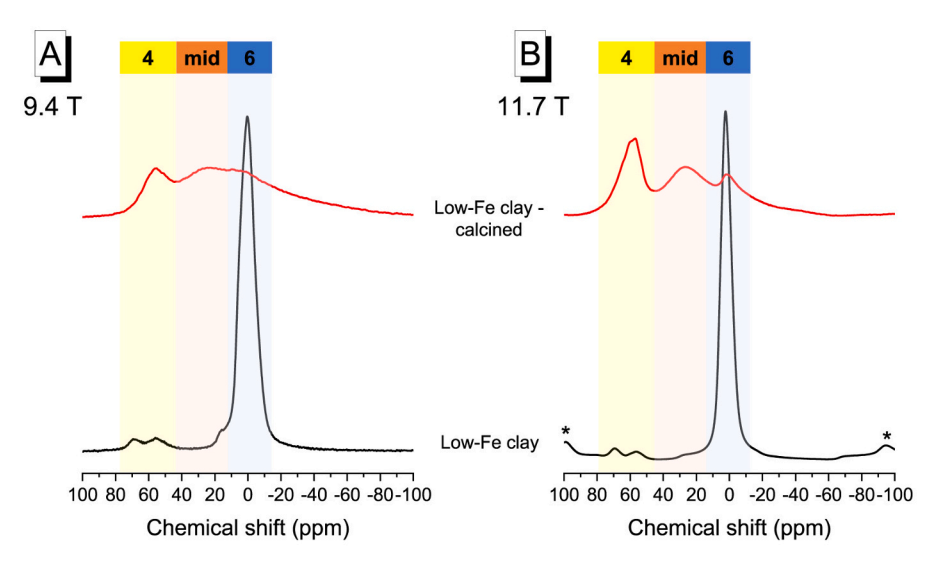


**Fig. 3.** <sup>27</sup>Al MAS NMR spectra for the low-Fe clay before and after calcination. Annotated numbers show corresponding Al coordination state(s), with "mid" denoting the mid-range Al resonance. The two figures present data collected on a (A) 9.4 T spectrometer, and a (B) 11.7 T spectrometer. \* symbols indicate the location of spinning side-bands.

Table 3

Proportions of Al coordination states in metakaolins reported in previous studies. The values stated for this study are the average from the data obtained at  $B_0=9.4\ T$  and the data obtained at  $B_0=11.7\ T$ . \*The calcination temperatures for the range of calcined clays used by Sankar et al. (2019) are unknown, as these were all industrially sourced.

Study	Calcination temperature (°C)	Field strength, B <sub>0</sub> (T)	4-fold Al (%)	5-fold Al / mid-range resonance (%)	6-fold Al (%)
Lambert et al. (1989)	600–850	11.7	32	52	10
Rocha and Klinowski, 1990b	750	Not stated	40	40	20
Massiot et al. (1995)	850	8.4	60	30	10
Izadifar et al. (2020)	700	9.4	10	50	40
Sankar et al. (2019)	Unknown*	7.05, 17.6	23–48	32–70	5-58
This study	750	9.4, 11.7	$\begin{array}{c} 37.7 \\ \pm \ 2.8 \end{array}$	$39.7 \pm 0.4$	$\begin{array}{c} 22.6 \\ \pm \ 3.1 \end{array}$

scale of the crystallographic unit cell, the visible changes in particle stacking in TEM images are relatively modest (Fig. 5). Whilst there does seem to be some evidence of subtle disruption in stacking, there was no dramatic change in particle morphology. These observations align with previous studies of kaolinite calcination via TEM (Bergaya et al., 1996) and optical microscopy (Romero and Garg, 2022), which show that dehydroxylation induces a minor reduction in layer thickness and

stacking faults, but does not cause extensive delamination.

Al K-edge EEL spectra of the low-Fe clays have the expected shape or profile of kaolinite (Hansen et al., 1994)); spectra were normalised to the main K-edge peak of kaolinite (at 1575 eV at the as-acquired energy calibration) in order to more clearly observe the differences in Al K-edge profile between samples (Fig. 6). In the previous sections, the term "midrange" resonance was used to describe the central resonance in the <sup>27</sup>Al MAS-NMR spectra, given uncertainty over its assignment to either 5-fold Al or 4-fold Al in a highly disordered environment. For the EEL spectra, 4-fold and 5-fold Al will be referred to specifically, as the previously mentioned debate does not readily translate to EEL spectra. The calcined low-Fe clay's spectrum showed a clear increase in relative intensity in the onset region of the edge profile (~1566 eV onwards) in comparison to the as-received low-Fe clay. This earlier edge onset coupled with an increase in intensity in this region and a drop in intensity of the first major feature relative to the high energy tail of the edge is due to a shift to Al in tetrahedral rather than octahedral co-ordination (Hansen et al., 1994). The change in edge profile can be attributed to a decrease in size of the Al co-ordination shell and loss of inversion symmetry leading to a wider variety of possible final electron states accessible for Al in tetrahedral rather than octahedral co-ordination. Such a 'fingerprint' for an increase in intensity at the Al K-edge onset upon the transition from 6 to 4-fold Al co-ordination has also been demonstrated by Al K-edge X-ray Absorption Spectroscopy (XAS) for a range of aluminosilicate minerals including kaolinite (Li et al., 1995; Ildefonse et al., 1998). The change of Al co-ordination after calcination was consistent with the observations from the <sup>27</sup>Al MAS NMR spectra (Fig. 3). However, whilst the measured EELS Al K-edges can easily distinguish between 6-fold and 4/5-fold Al co-ordination, they do not readily distinguish 4-fold from 5-fold Al coordination (this parallels Liao et al. (2020) who were unable to

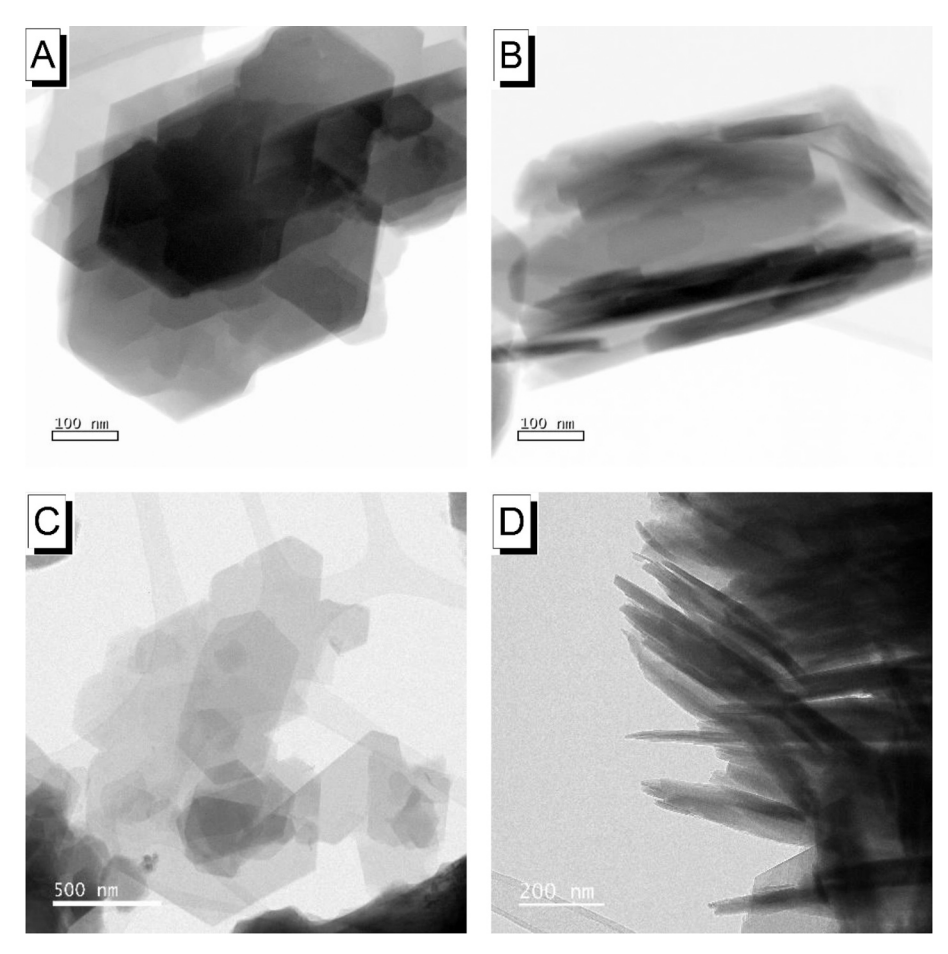
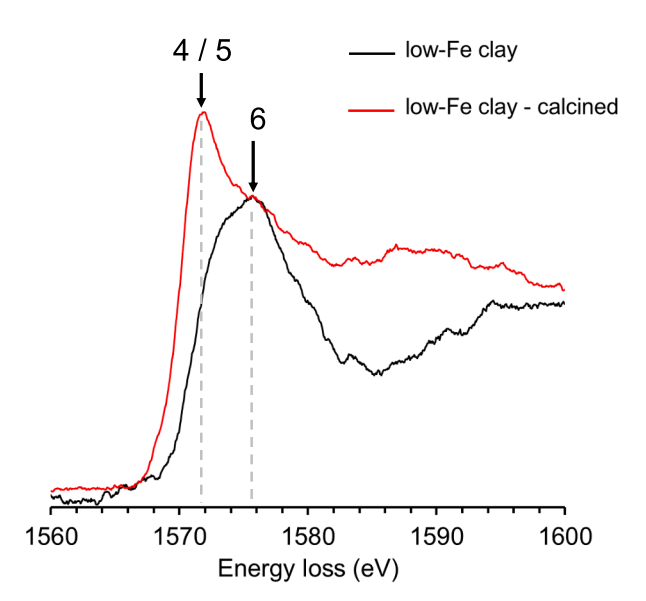


Fig. 5. TEM images showing kaolinite particles in a, b) the as-received low-Fe clay, and c, d) the calcined low-Fe clay.



**Fig. 6.** EEL spectra, normalised to the kaolinite peak intensity at 1575 eV, for the low-Fe clay in both as-received and calcined states. Annotated numbers show corresponding Al coordination state(s).

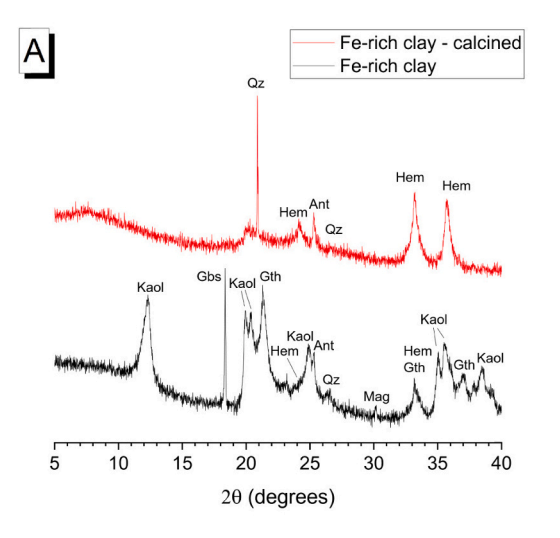
uniquely identify 5-fold Al co-ordination in aluminosilicate glasses using STEM-EELS at the Al *L*-edge).

#### 3.2. Characterisation of Fe-rich clays

The as-received Fe-rich clay exhibited more complex mineralogy compared to the as-received low-Fe clay. Alongside kaolinite (PDF# 01–079-1570), a substantial proportion of goethite (FeO(OH)) (PDF# 01–073-63,522), was present, along with minor amounts of quartz (PDF# 00–046-1045), hematite (Fe<sub>2</sub>O<sub>3</sub>) (PDF #00–033-0664), magnetite (Fe<sub>3</sub>O<sub>4</sub>) (PDF 00–019-0629), gibbsite (Al(OH<sub>3</sub>)) (PDF# 01–070-2038) and anatase (TiO<sub>2</sub>) (PDF# 00–021-1271) (Fig. 7a). Using the approach described in Eq. 1, the kaolinite content was confirmed to be  $\sim$ 55 wt%. The kaolinite 001 reflection at 12.3°20 (corresponding to a basal spacing of 7.2 Å) in the Fe-rich clay was broader compared to that in the low-Fe clay (Fig. 2a), suggestive of a smaller particle size and/or more disordered crystal structure (Brindley and Brown, 1980), as was

previously observed for kaolinitic clays of lateritic origin (Kaze et al., 2017). The presence of some halloysite-(7 Å) cannot be ruled out, as its diffraction pattern is similar to that of a disordered kaolinite and has reported to be present in the lithomarge layer of the Interbasaltic Formation at some depths (Hill et al., 2000). Halloysite-(7 Å) refers to the dehydrated form of halloysite (Al<sub>2</sub>Si<sub>2</sub>O<sub>5</sub>) in line with AIPEA recommended nomenclature (Guggenheim et al., 2006). However, given the structural and chemical similarities between disordered kaolinite and halloysite-(7 Å), they are very difficult to distinguish (Joussein et al., 2005). The basal spacing (7.2 Å) of the 001 reflection in the low-Fe and Fe-rich clays indicates that the majority of the clay mineral content in the Fe-rich clay is likely to be kaolinite, as halloysite-(7 Å) typically has a slightly higher basal spacing in the range of 7.2–7.6 Å (Joussein et al., 2005). Another factor likely contributing to the broader reflections and higher signal-to-noise ratio of the Fe-rich clays' diffraction patterns (compared to the low-Fe clays' patterns) was Fe—K fluorescence arising from the substantial quantity of Fe (hydr)oxides and/or oxides present in the Fe-rich clavs (Brown and Wood, 1985). After calcination, the kaolinite 001 reflection in the Fe-rich clay XRD pattern was no longer detectable. A small, broad reflection at 20.4°20 was observed in the pattern of the calcined Fe-rich clay. Amongst the associated minerals, goethite and magnetite underwent a thermal decomposition to form hematite. The TG curve for the as-received Fe-rich clay (Fig. 7b) showed the dehydroxylation of kaolinite in the temperature range of 300-600 °C, and the thermal decomposition of goethite in the temperature range of 200-350 °C (Földvári, 2011). The TG curve of the Fe-rich clay has a similar profile to the TG curves of other lateritic clays containing kaolinite and goethite, with the lower dehydroxylation temperature of the Fe-rich clay (relative to the low-Fe clay) attributed to the greater extent of structural disorder of kaolinite in the Fe-rich clay (Kaze et al., 2017). For the calcined Fe-rich clay, negligible mass loss was observed over 300-600 °C, indicating that dehydroxylation was complete after calcination at 750  $^{\circ}$ C (consistent with the low Fe clays).

The TEM images of the un-calcined Fe-rich clay (Fig. 8a) showed a noticeably smaller size of individual particles (but not agglomerates) compared to the low-Fe clay (Fig. 5a). These fine-scale observations are in agreement with bulk measurements of specific surface area: the Ferich clay had a much higher specific surface area (59.8  $\rm m^2 g^{-1}$ ) than the low-Fe clay (6.7  $\rm m^2 g^{-1}$ ), despite the Fe-rich clay having a slightly lower kaolinite content (see Table S1 in Supplementary Information). These pieces of evidence support the interpretation of the greater width of the 001 kaolinite reflection in the XRD pattern of the Fe-rich clay, relative to the low-Fe clay, being partly due to the Fe-rich clay's fine



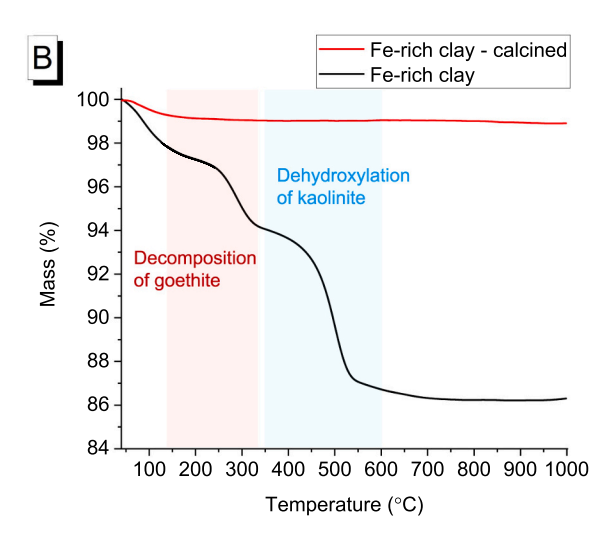


Fig. 7. a) XRD patterns and b) TG curves of the Fe-rich clay, before (black) and after (red) calcination. Ant = anatase; Gbs = gibbsite; Gth = goethite; Hem = hematite; Kaol = kaolinite; Mag = magnetite; Qz = quartz. (For interpretation of the references to colour in this figure legend, the reader is referred to the web version of this article.)

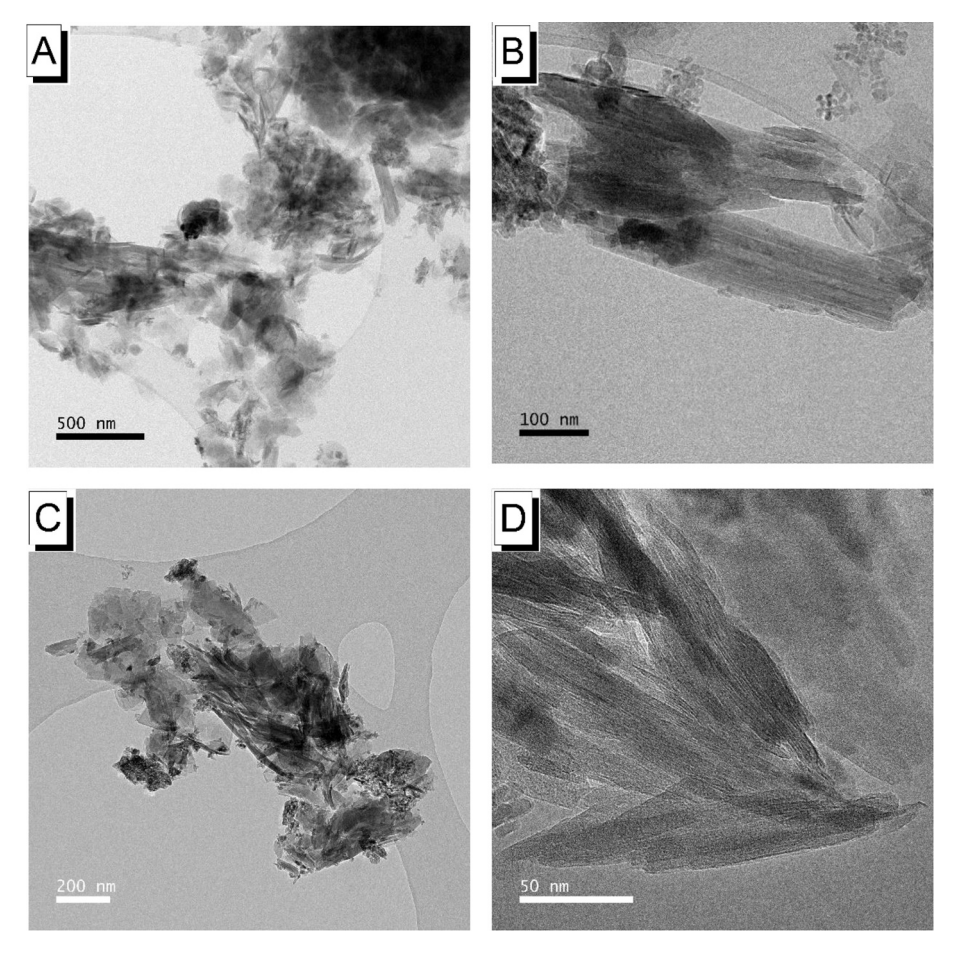


Fig. 8. TEM images showing kaolinite particles in a, b) the as-received Fe-rich clay, and c, d) the calcined Fe-rich clay.

kaolinite particle size (Fig. 2b). The plate-like morphology of the stacked particles is indicative of disordered kaolinite; however, the presence of some particles of halloysite-(7 Å) with a plate-like or elongated tubular

morphology cannot be excluded. Similar to the low-Fe clays, calcination had a modest disruptive effect on stacking of kaolinite particles in the calcined Fe-rich clay (Fig. 8d) compared to the raw Fe-rich clay

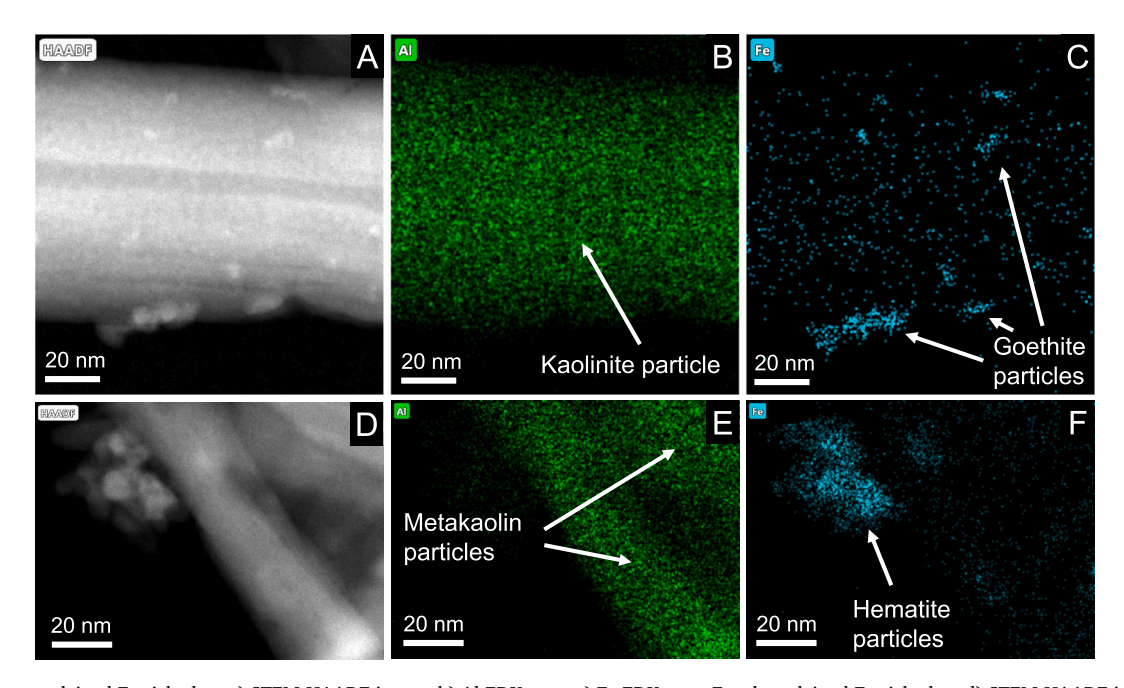


Fig. 9. For the non-calcined Fe-rich clay: a) STEM-HAADF image; b) Al EDX map; c) Fe EDX map. For the calcined Fe-rich clay: d) STEM-HAADF image; e) Al EDX map; f) Fe EDX map. Images show very fine particles of Fe-based mineral adhered to platy kaolinite or meta-kaolinite particles.

(Fig. 8b).

STEM-EDX maps showed that the Fe-based mineral particles (predominantly goethite, as identified by XRD in Fig. 7a) were present as very fine particles. The fine goethite particles were adhered to the surface of kaolinite particles, which are themselves distinguished by their high Al content by EDX spectroscopy and platy morphology (Fig. 9a-c). Fe-based minerals can exist in a variety of sizes depending on formation and weathering processes, including as very fine particles which can be adhered to the surfaces of clay mineral particles (Jefferson et al., 1975; Fritsch et al., 2002). Substitution of Fe for octahedral Al in kaolinite can occur depending on its weathering route (Herbillon et al., 1976), but the extent of substitution is limited to a minor percentage, estimated as <4% (Herbillon et al., 1976). Within this range, lateritic kaolinites have a relatively high proportion of Fe substitution in comparison to kaolinites formed via other routes (Mendelovici et al., 1979). Therefore, whilst octahedral Fe in kaolinite may have accounted for the weak Fe signal observed in the areas corresponding to kaolinite platelets (Fig. 9c), the particles which exhibited a strong Fe signal were confidently identified as Fe-based minerals. In the calcined Fe-rich clay, Fe-based minerals (predominantly hematite, as identified via XRD in Fig. 7a) were still present as very fine particles after the thermal decomposition of goethite to hematite (Fig. 9f).

EEL spectra of the Fe-rich clays were normalised to the main Al Kedge peak of kaolinite as described previously in Section 3.1 (Fig. 10). The kaolinite in the Fe-rich clay contained a greater proportion of 4/5fold Al than the kaolinite in the low-Fe clay, on the basis of the higher intensity at the edge onset (1572 eV) of the Fe-rich clay's spectrum (Fig. 6 vs Fig. 10). A higher proportion of 4/5-fold Al is consistent with the lateritic origins of the Fe-rich clay being more conducive to structural disorder in kaolinite (Fritsch et al., 2002; Balan et al., 2007), in comparison to the more ordered kaolinite expected from the mixed residual and hydrothermal origins of the low-Fe clay (Murray, 2006). In the calcined clay's spectrum, there was an increase in relative intensity at the onset of the Al K-edge profile, associated with an increase in 4- and 5-fold Al (relative to the as-received clay's spectrum). A greater change in Al K-edge profile upon calcination was observed for the low-Fe clay than the calcined Fe-rich clay. A lower 4/5-fold Al content of the calcined Fe-rich clay compared to the calcined low-Fe clay is plausible, given the known variation in Al distribution between different metakaolins (Sankar et al., 2019). Halloysite-(7 Å), which could be present to some extent in the Fe-rich clay, exhibits very similar Al coordination to kaolinite both before and after calcination (Smith et al., 1993; Zhang et al., 2022), and so would not be expected to significantly change the EEL spectra if present.

Whilst the line profile of the Al *K*-edge can distinguish between 6-fold and 4/5-fold Al, a limitation is that it cannot readily distinguish between 4-fold and 5-fold Al. Nonetheless, there is still uncertainty about whether 5-fold Al truly exists in meta-kaolinite, therefore a combined measured of 4/5-fold Al is still informative. However, EELS could be used to more quantitatively determine 6:4/5-fold Al ratios by fitting of reference spectra acquired by additional <sup>27</sup>Al MAS NMR and EELS measurement of pure kaolinite and meta kaolinite standards.

Future research should also explore the influence of Al coordination state on the chemical reactivity of calcined Fe-rich clays, alongside other determining factors such as total meta-kaolinite content and particle size. There is potential to use in-situ diffraction techniques in the STEM to understand the changes in layer structure and local ordering that occur upon calcination in Fe-rich clays. STEM-EELS can also investigate novel processing routes of Fe-rich clays, such as mechano-chemical activation or microwave-based calcination. This can improve our understanding of the structure-processing-properties relationships around using Fe-rich clays in cementitious systems.

#### 4. Conclusions

This study shows that Al K-edge EELS can be used to identify changes

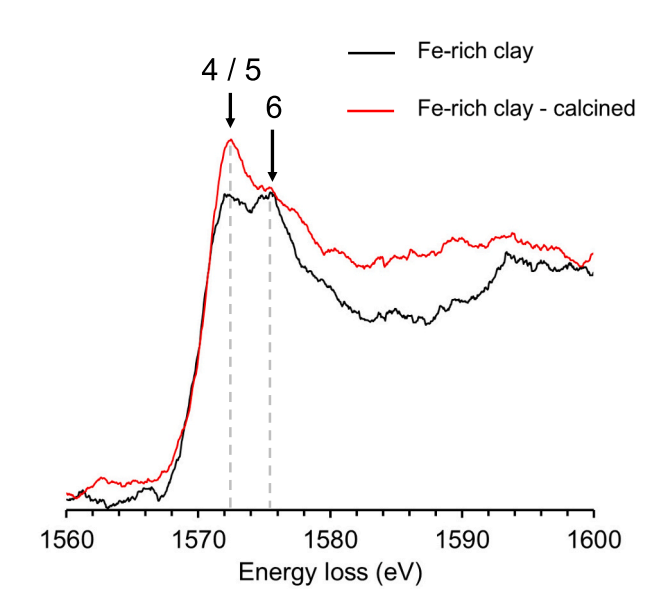


**Fig. 10.** EEL spectra, normalised to the kaolinite peak intensity at 1575 eV, for the Fe-rich clay in both as-received and calcined states. Annotated numbers show corresponding Al coordination state(s).

in Al co-ordination of kaolinite upon calcination and transformation to meta-kaolinite. This has been demonstrated for an Fe-rich clay whose Fe content is too high to yield meaningful data using <sup>27</sup>Al MAS NMR. This capability gives EELS clear value in the study of Fe-rich clays. EELS also revealed differences in octahedral and tetrahedral substitutions between the low-Fe clay and the Fe-rich clay, consistent with their different geological formation routes.

# CRediT authorship contribution statement

Alastair T.M. Marsh: Writing – original draft, Supervision, Resources, Project administration, Investigation, Funding acquisition, Conceptualization. Andy P. Brown: Writing – review & editing, Methodology, Investigation. Helen M. Freeman: Methodology, Investigation. Brant Walkley: Writing – review & editing, Methodology, Investigation, Funding acquisition. Helen Pendlowski: Methodology, Investigation. Susan A. Bernal: Writing – review & editing, Supervision, Resources, Funding acquisition.

### Declaration of competing interest

The authors declare that they have no known competing financial interests or personal relationships that could have appeared to influence the work reported in this paper.

# Data availability

Data created during this research are openly available from the White Rose Research Online data repository at <a href="https://doi.org/10.5518/1531">https://doi.org/10.5518/1531</a>

# Acknowledgements

This study was sponsored via the White Rose Collaboration Fund project "Enhancing analytical capabilities in soils for low-carbon technologies", and an EPSRC Early Career Fellowship (EP/R001642/1). Thanks are given to Vicky Leadley and Dan Geddes for assistance with <sup>27</sup>Al MAS NMR measurements, and Sreejith Krishnan for advice about XRD analysis. Thanks are also given to Martin Stennett, Mark Hodson,

Rob Mills, Amy Wright and Anke Neumann for helpful discussions around clay characterisation. Data created during this research are openly available from the White Rose Research Online data repository at https://doi.org/10.5518/1531.

#### Appendix A. Supplementary data

Supplementary data to this article can be found online at https://doi.org/10.1016/j.clay.2024.107402.

#### References

- Alujas Diaz, A., Almenares Reyes, R.S., Hanein, T., Irassar, E.F., Juenger, M., Kanavaris, F., Maier, M., Marsh, A.T., Sui, T., Thienel, K.-C., Valentini, L., Wang, B., Zunino, F., Snellings, R., 2022. Properties and occurrence of clay resources for use as supplementary cementitious materials: a paper of RILEM TC 282-CCL. Mater. Struct. 55, 139. https://doi.org/10.1617/s11527-022-01972-2.
- Andrini, L., Gauna, M.R., Conconi, M.S., Suarez, G., Requejo, F.G., Aglietti, E.F., Rendtorff, N.M., 2016. Extended and local structural description of a kaolinitic clay, its fired ceramics and intermediates: an XRD and XANES analysis. Appl. Clay Sci. 124-125, 39–45. https://doi.org/10.1016/j.clay.2016.01.049.
- Balan, E., Fritsch, E., Allard, T., Calas, G., 2007. Inheritance vs. neoformation of kaolinite during lateritic soil formation: a case study in the middle Amazon Basin. Clay Clay Miner. 55, 253–259. https://doi.org/10.1346/CCMN.2007.0550303.
- Beauvais, A., 1999. Geochemical balance of lateritization processes and climatic signatures in weathering profiles overlain by ferricretes in Central Africa. Geochim. Cosmochim. Acta 63, 3939–3957. https://doi.org/10.1016/S0016-7037(99)00173-8
- Bergaya, F., Dion, P., Alcover, J.F., Clinard, C., Tchoubar, D., 1996. TEM study of kaolinite thermal decomposition by controlled-rate thermal analysis. J. Mater. Sci. 31, 5069–5075. https://doi.org/10.1007/BF00355907.
- Bish, D.L., Von Dreele, R.B., 1989. Rietveld Refinement of Non-Hydrogen Atomic Positions in Kaolinite. Clay Clay Miner. 37, 289–296. https://doi.org/10.1346/ CCMN 1989 0370401
- Brigatti, M.F., Galan, E., Theng, B.K.G., 2006. Chapter 2 Structures and Mineralogy of Clay Minerals. In: Bergaya, F., Theng, B.K.G., Lagaly, G. (Eds.), Developments in Clay Science. Elsevier, pp. 19–86. https://doi.org/10.1016/S1572-4352(05)01002-0.
- Brindley, G.W., Brown, G., 1980. Crystal Structures of Clay Minerals and their X-Ray Identification. The Mineralogical Society of Great Britain and Ireland, London, U.K.
- Brindley, G.W., Kao, C.-C., Harrison, J.L., Lipsicas, M., Raythatha, R., 1986. Relation between Structural Disorder and Other Characteristics of Kaolinites and Dickites. Clay Clay Miner. 34, 239–249. https://doi.org/10.1346/CCMN.1986.0340303.
- Brown, G., Wood, I.G., 1985. Estimation of iron oxides in soil clays by profile refinement combined with differential X-ray diffraction. Clay Miner. 20, 15–27. https://doi.org/ 10.1180/claymin.1985.020.1.02.
- Butler, B.M., Hillier, S., 2021. Automated full-pattern summation of X-ray powder diffraction data for high-throughput quantification of clay-bearing mixtures. Clay Clay Miner. 69, 38–51. https://doi.org/10.1007/s42860-020-00105-6.
- Day-Stirrat, R.J., Aplin, A.C., Kurtev, K.D., Schleicher, A.M., Brown, A.P., Środoń, J., 2017. Late diagenesis of illite-smectite in the Podhale Basin, southern Poland: Chemistry, morphology, and preferred orientation. Geosphere 13, 2137–2153. https://doi.org/10.1130/GES01516.1.
- d'Espinose de Lacaillerie, J.-B., Fretigny, C., Massiot, D., 2008. MAS NMR spectra of quadrupolar nuclei in disordered solids: the Czjzek model. J. Magn. Reson. 192, 244–251. https://doi.org/10.1016/j.jmr.2008.03.001.
- Egerton, R.F., 2008. Electron energy-loss spectroscopy in the TEM. Rep. Prog. Phys. 72, 016502 https://doi.org/10.1088/0034-4885/72/1/016502.
- Exley, C.S., 1976. Observations on the formation of kaolinite in the St. Austell granite, Cornwall. Clay Miner. 11, 51–63. https://doi.org/10.1180/claymin.1976.011.1.06.
- Fabbri, B., Gualtieri, S., Leonardi, C., 2013. Modifications induced by the thermal treatment of kaolin and determination of reactivity of metakaolin. Appl. Clay Sci. 73, 2–10. https://doi.org/10.1016/j.clay.2012.09.019.
- Földvári, M., 2011. Handbook of Thermogravimetric System of Minerals and its Use in Geological Practice. Geological Institute of Hungary, Budapest.
- Freeman, H.M., Perez, J.P.H., Hondow, N., Benning, L.G., Brown, A.P., 2019. Beam-induced oxidation of mixed-valent Fe (oxyhydr)oxides (green rust) monitored by STEM-EELS. Micron 122, 46–52. https://doi.org/10.1016/j.micron.2019.02.002.
- Fritsch, E., Montes-Lauar, C.R., Boulet, R., Melfi, A.J., Balan, E., Magat, P., 2002. Lateritic and redoximorphic features in a faulted landscape near Manaus, Brazil. Eur. J. Soil Sci. 53, 203–217. https://doi.org/10.1046/j.1351-0754.2002.00448.x.
- Garvie, L.A.J., Zega, T.J., Rez, P., Buseck, P.R., 2004. Nanometer-scale measurements of Fe3+/ΣFe by electron energy-loss spectroscopy: A cautionary note, 89, pp. 1610–1616. https://doi.org/10.2138/am-2004-11-1204.
- Giraudeau, P., Tea, I., Remaud, G.S., Akoka, S., 2014. Reference and normalization methods: Essential tools for the intercomparison of NMR spectra. J. Pharm. Biomed. Anal. 93, 3–16. https://doi.org/10.1016/j.jpba.2013.07.020.
- Gualtieri, A., Bellotto, M., 1998. Modelling the structure of the metastable phases in the reaction sequence kaolinite-mullite by X-ray scattering experiments. Phys. Chem. Miner. 25, 442–452. https://doi.org/10.1007/s002690050134.
- Guggenheim, S., Bain, D.C., Bergaya, F., Brigatti, M.F., Drits, V.A., Eberl, D.D., Formoso, M.L.L., Galán, E., Merriman, R.J., Peacor, D.R., Stanjek, H., Watanabe, T., 2002. Report of the Association Internationale pour l'Etude des Argiles (AIPEA)

- Nomenclature Committee for 2001: Order, disorder and crystallinity in phyllosilicates and the use of the 'Crystallinity Index'. Clay Miner. 37, 389–393. https://doi.org/10.1180/0009855023720043.
- Guggenheim, S., Adams, J.M., Bain, D.C., Bergaya, F., Brigatti, M.F., Drits, V.A., Formoso, M.L.L., Galán, E., Kogure, T., Stanjek, H., 2006. Summary of recommendations of Nomenclature committees relevant to clay mineralogy: Report of the association Internationale pour l'Etude des Argiles (AIPEA) Nomenclature Committee for 2006. Clay Clay Miner. 54, 761–772. https://doi.org/10.1346/CCMN.2006.0540610.
- Hansen, P.L., Brydson, R., McComb, D.W., Richardson, I., 1994. EELS fingerprint of Alcoordination in silicates. Microsc. Microanal. Microstruct. 5, 173–182.
- Hayashi, S., Ueda, T., Hayamizu, K., Akiba, E., 1992. NMR study of kaolinite. 1. Silicon-29, aluminum-27, and proton spectra. J. Phys. Chem. 96, 10922–10928. https://doi. org/10.1021/j100205a058.
- Heller-Kallai, L., 2006. Chapter 7.2 thermally modified clay minerals. In: Bergaya, F., Theng, B.K.G., Lagaly, G. (Eds.), Developments in Clay Science. Elsevier, pp. 289–308. https://doi.org/10.1016/S1572-4352(05)01009-3.
- Herbillon, A.J., Mestdagh, M.M., Vielvoye, L., Derouane, E.G., 1976. Iron in kaolinite with special reference to kaolinite from tropical soils. Clay Miner. 11, 201–220. https://doi.org/10.1180/claymin.1976.011.3.03.
- Hill, I.G., Worden, R.H., Meighan, I.G., 2000. Geochemical evolution of a palaeolaterite: the Interbasaltic Formation, Northern Ireland. Chem. Geol. 166, 65–84. https://doi. org/10.1016/S0009-2541(99)00179-5.
- Ildefonse, P., Cabaret, D., Sainctavit, P., Calas, G., Flank, A.M., Lagarde, P., 1998. Aluminium X-ray absorption near Edge Structure in model compounds and Earth's surface minerals. Phys. Chem. Miner. 25, 112–121. https://doi.org/10.1007/ s002690050093.
- Imerys Kaolin, 2019. Polwhite E Technical Data Sheet.
- Izadifar, M., Thissen, P., Steudel, A., Kleeberg, R., Kaufhold, S., Kaltenbach, J., Schuhmann, R., Dehn, F., Emmerich, K., 2020. Comprehensive examination of dehydroxylation of kaolinite, disordered kaolinite, and dickite: experimental studies and density functional theory. Clay Clay Miner. https://doi.org/10.1007/s42860-020-00082-w
- Jefferson, D.A., Tricker, M.J., Winterbottom, A.P., 1975. Electron-microscopic and mössbauer spectroscopic studies of iron-stained kaolinite minerals. Clay Clay Miner. 23, 355–360. https://doi.org/10.1346/CCMN.1975.0230505.
- Joussein, E., Petit, S., Churchman, J., Theng, B., Righi, D., Delvaux, B., 2005. Halloysite clay minerals — a review. Clay Miner. 40, 383–426. https://doi.org/10.1180/ 0009855054040180.
- Kaze, R.C., Beleuk, A., Moungam, L.M., Fonkwe Djouka, M.L., Nana, A., Kamseu, E., Chinje Melo, U.F., Leonelli, C., 2017. The corrosion of kaolinite by iron minerals and the effects on geopolymerization. Appl. Clay Sci. 138, 48–62. https://doi.org/ 10.1016/j.clay.2016.12.040.
- Kaze, C.R., Lecomte-Nana, G.L., Kamseu, E., Camacho, P.S., Yorkshire, A.S., Provis, J.L., Duttine, M., Wattiaux, A., Melo, U.C., 2021. Mechanical and physical properties of inorganic polymer cement made of iron-rich laterite and lateritic clay: a comparative study. Cem. Concr. Res. 140, 106320 https://doi.org/10.1016/j. cemconres 2020 106320
- Khalifa, A.Z., Cizer, Ö., Pontikes, Y., Heath, A., Patureau, P., Bernal, S.A., Marsh, A.T.M., 2020. Advances in alkali-activation of clay minerals. Cem. Concr. Res. 132, 106050 https://doi.org/10.1016/j.cemconres.2020.106050.
- Kinsey, R.A., Kirkpatrick, R.J., Hower, J., Smith, K.A., Oldfield, E., 1985. High resolution aluminum-27 and silicon-29 nuclear magnetic resonance spectroscopic study of layer silicates, including clay minerals. Am. Mineral. 70, 537–548.
- Kirkpatrick, R.J., Smith, K.A., Schramm, S., Turner, G., Yang, W.-H., 1985. Solid-STATE nuclear magnetic resonance spectroscopy of minerals. Annu. Rev. Earth Planet. Sci. 13, 29–47. https://doi.org/10.1146/annurev.ea.13.050185.000333. Komadel, P., Madejová, J., 2006. Chapter 7.1 acid activation of clay minerals. In:
- Komadel, P., Madejová, J., 2006. Chapter 7.1 acid activation of clay minerals. In: Bergaya, F., Theng, B.K.G., Lagaly, G. (Eds.), Developments in Clay Science. Elsevier, pp. 263–287. https://doi.org/10.1016/S1572-4352(05)01008-1.
- Kuenzel, C., Neville, T.P., Donatello, S., Vandeperre, L., Boccaccini, A.R., Cheeseman, C. R., 2013. Influence of metakaolin characteristics on the mechanical properties of geopolymers. Appl. Clay Sci. 83-84, 308–314. https://doi.org/10.1016/j.clay.2013.08.023.
- Lambert, J.F., Millman, W.S., Fripiat, J.J., 1989. Revisiting kaolinite dehydroxylation: a silicon-29 and aluminum-27 MAS NMR study. J. Am. Chem. Soc. 111, 3517–3522. https://doi.org/10.1021/ja00192a005.
- Li, D., Bancroft, G.M., Fleet, M.E., Feng, X.H., Pan, Y., 1995. Al K-edge XANES spectra of aluminosilicate minerals. Am. Mineral. 80, 432–440. https://doi.org/10.2138/am-1995.5.602
- Liao, K., Masuno, A., Taguchi, A., Moriwake, H., Inoue, H., Mizoguchi, T., 2020. Revealing spatial distribution of al-coordinated species in a phase-separated aluminosilicate glass by STEM-EELS. J. Phys. Chem. Lett. 11, 9637–9642. https://doi.org/10.1021/acs.jpclett.0c02687.
- Lippmaa, E., Samoson, A., Magi, M., 1986. High-resolution aluminum-27 NMR of aluminosilicates. J. Am. Chem. Soc. 108, 1730–1735. https://doi.org/10.1021/ ia00268a002.
- Mackenzie, R.C., Caillère, S., 1975. The thermal characteristics of soil minerals and the use of these characteristics in the qualitative and quantitative determination of clay minerals in soils. In: Gieseking, J.E. (Ed.), Soil Components, Inorganic Components, vol. 2. Springer Berlin Heidelberg, Berlin, Heidelberg, pp. 529–571. https://doi.org/ 10.1007/978-3-642-65917-1\_16.
- MacKenzie, K.J.D., Brown, I.W.M., Meinhold, R.H., Bowden, M.E., 1985. Outstanding Problems in the Kaolinite-Mullite Reaction Sequence Investigated by 29Si and 27Al Solid-state Nuclear magnetic Resonance: I, Metakaolinite. J. Am. Ceram. Soc. 68, 293–297. https://doi.org/10.1111/j.1151-2916.1985.tb15228.x.

- Mackenzie, K.J.D., Brown, I.W.M., Cardile, C.M., Meinhold, R.H., 1987. The thermal reactions of muscovite studied by high-resolution solid-state 29-Si and 27-AI NMR. J. Mater. Sci. 22, 2645–2654. https://doi.org/10.1007/BF01082158.
- Mantovani, M., Escudero, A., Becerro, A.I., 2009. Application of 29Si and 27Al MAS NMR spectroscopy to the study of the reaction mechanism of kaolinite to illite/muscovite. Clay Clay Miner. 57, 302–310. https://doi.org/10.1346/CCMN.2009.0570303.
- Massiot, D., Dion, P., Alcover, J.F., Bergaya, F., 1995. 27Al and 29Si MAS NMR Study of Kaolinite thermal Decomposition by Controlled Rate thermal Analysis. J. Am. Ceram. Soc. 78, 2940–2944. https://doi.org/10.1111/j.1151-2916.1995.tb09067.x.
- Massiot, D., Fayon, F., Capron, M., King, I., Le Calvé, S., Álonso, B., Durand, J.-O., Bujoli, B., Gan, Z., Hoatson, G., 2002. Modelling one- and two-dimensional solidstate NMR spectra. Magn. Reson. Chem. 40, 70–76. https://doi.org/10.1002/ mrc.984.
- McIntosh, A., Lawther, S.E.M., Kwasny, J., Soutsos, M.N., Cleland, D., Nanukuttan, S., 2015. Selection and characterisation of geological materials for use as geopolymer precursors. Adv. Appl. Ceram. 114, 378–385. https://doi.org/10.1179/ 1743676115Y.0000000055.
- McManus, J., Ashbrook, S.E., MacKenzie, K.J.D., Wimperis, S., 2001. 27Al multiple-quantum MAS and 27Al{1H} CPMAS NMR study of amorphous aluminosilicates. J. Non-Cryst. Solids 282, 278–290. https://doi.org/10.1016/S0022-3093(01)00313-1
- Mendelovici, E., Yariv, S., Villalba, R., 1979. Iron-bearing kaolinite in Venezuelan laterites: I. Infrared spectroscopy and chemical dissolution evidence. Clay Miner. 14, 323–331. https://doi.org/10.1180/claymin.1979.014.4.08.
- Mestdagh, M.M., Vielvoye, L., Herbillon, A.J., 1980. Iron in kaolinite: II. The relationship between kaolinite crystallinity and iron content. Clay Miner. 15, 1–13. https://doi. org/10.1180/claymin.1980.015.1.01.
- Murray, H.H., 2006. Chapter 3 geology and location of major industrial clay deposits. In: Murray, H.H. (Ed.), Developments in Clay Science. Elsevier, pp. 33–65. https://doi. org/10.1016/S1572-4352(06)02003-4.
- Newman, R.H., Childs, C.W., Churchman, G.J., 1994. Aluminium coordination and structural disorder in halloysite and kaolinite by 27Al NMR spectroscopy. Clay Miner. 29, 305–312. https://doi.org/10.1180/claymin.1994.029.3.01.
- Omotoso, O., McCarty, D.K., Hillier, S., Kleeberg, R., 2006. Some successful approaches to quantitative mineral analysis as revealed by the 3rd Reynolds Cup contest. Clay Clay Miner. 54, 748–760. https://doi.org/10.1346/CCMN.2006.0540609.
- Pan, Y.-H., Vaughan, G., Brydson, R., Bleloch, A., Gass, M., Sader, K., Brown, A., 2010. Electron-beam-induced reduction of Fe3+ in iron phosphate dihydrate, ferrihydrite, haemosiderin and ferritin as revealed by electron energy-loss spectroscopy. Ultramicroscopy 110, 1020–1032. https://doi.org/10.1016/j.ultramic.2010.01.008.
- Paris, M., 2014. The two aluminum sites in the 27Al MAS NMR spectrum of kaolinite: Accurate determination of isotropic chemical shifts and quadrupolar interaction parameters. Am. Mineral. 99, 393–400. https://doi.org/10.2138/am.2014.4607.
- Psyrillos, A., Manning David, A., Burley Stuart, D., 1998. Geochemical constraints on kaolinization in the St Austell Granite, Cornwall, England. J. Geol. Soc. Lond. 155, 829–840. https://doi.org/10.1144/esigs.155.5.0829.
- Rocha, J., 1999. Single- and Triple-Quantum 27Al MAS NMR Study of the thermal Transformation of Kaolinite. J. Phys. Chem. B 103, 9801–9804. https://doi.org/ 10.1021/jn991516b
- Rocha, J., Klinowski, J., 1990a. Solid-State NMR Studies of the Structure and Reactivity of Metakaolinite. Angew. Chem. 29, 553–554. https://doi.org/10.1002/ anie.199005531.

- Rocha, J., Klinowski, J., 1990b. 29Si and 27Al magic-angle-spinning NMR studies of the thermal transformation of kaolinite. Phys. Chem. Miner. 17, 179–186. https://doi. org/10.1007/BF00199671.
- Romero, P., Garg, N., 2022. Evolution of kaolinite morphology upon exfoliation and dissolution: evidence for nanoscale layer thinning in metakaolin. Appl. Clay Sci. 222, 106486 https://doi.org/10.1016/j.clay.2022.106486.
- Sankar, K., Sutrisno, A., Kriven, W.M., 2019. Slag-fly ash and slag-metakaolin binders: Part II—Properties of precursors and NMR study of poorly ordered phases. J. Am. Ceram. Soc. 102, 3204–3227. https://doi.org/10.1111/jace.16224.
- Schroeder, P.A., Pruett, R.J., 1996. Fe ordering in kaolinite: Insights from 29Si and 27Al MAS NMR spectroscopy. Am. Mineral. 81, 26–38. https://doi.org/10.2138/am-1996-1-204
- Scrivener, K., Martirena, F., Bishnoi, S., Maity, S., 2018. Calcined clay limestone cements (LC3). Cem. Concr. Res. 114, 49–56. https://doi.org/10.1016/j. cemconres 2017/08/017
- Smith, M.E., Neal, G., Trigg, M.B., Drennan, J., 1993. Structural characterization of the thermal transformation of halloysite by solid state NMR. Appl. Magn. Reson. 4, 157–170. https://doi.org/10.1007/BF03162561.
- Snellings, R., Reyes, R.A., Hanein, T., Irassar, E.F., Kanavaris, F., Maier, M., Marsh, A.T. M., Valentini, L., Zunino, F., Diaz, A.A., 2022. Paper of RILEM TC 282-CCL: Mineralogical characterization methods for clay resources intended for use as supplementary cementitious material. Mater. Struct. 55 https://doi.org/10.1617/s11527.072.01473.1
- Ufer, K., Raven, M.D., 2017. Application of the Rietveld Method in the Reynolds Cup Contest. Clay Clay Miner. 65, 286–297. https://doi.org/10.1346/ CCMN 2017.064063
- Walkley, B., Provis, J.L., 2019. Solid-state nuclear magnetic resonance spectroscopy of cements. Materi. Today Adv. 1, 100007 https://doi.org/10.1016/j. mtc.du/2010.100007
- White, C.E., Provis, J.L., Proffen, T., Riley, D.P., van Deventer, J.S.J., 2010. Combining density functional theory (DFT) and pair distribution function (PDF) analysis to solve the structure of metastable materials: the case of metakaolin. Phys. Chem. Chem. Phys. 12, 3239–3245. https://doi.org/10.1039/B922993K.
- White, C.E., Perander, L.M., Provis, J.L., van Deventer, J.S.J., 2011. The use of XANES to clarify issues related to bonding environments in metakaolin: a discussion of the paper S. Sperinck et al., "Dehydroxylation of kaolinite to metakaolin-a molecular dynamics study," J. Mater. Chem., 2011, 21, 2118–2125. J. Mater. Chem. 21, 7007–7010. https://doi.org/10.1039/CIJM10379B.
- Woodward, G.L., Peacock, C.L., Otero-Fariña, A., Thompson, O.R., Brown, A.P., Burke, I. T., 2018. A universal uptake mechanism for cobalt(II) on soil constituents: Ferrihydrite, kaolinite, humic acid, and organo-mineral composites. Geochim. Cosmochim. Acta 238, 270–291. https://doi.org/10.1016/j.gca.2018.06.035.
- Xiao, Y., James Kirkpatrick, R., Hay, R.L., Kim, Y.J., Phillips, B.L., 1995. Investigation of Al,Si order in K-feldspars using 27Al and 29Si MAS NMR. Mineral. Mag. 59, 47–61. https://doi.org/10.1180/minmag.1995.59.394.05.
- Zhang, B., Yu, T., Guo, H., Chen, J., Liu, Y., Yuan, P., 2022. Effect of the SiO2/Al2O3 molar ratio on the microstructure and properties of clay-based geopolymers: a comparative study of kaolinite-based and halloysite-based geopolymers. Clay Clay Miner. 70, 882–902. https://doi.org/10.1007/s42860-023-00223-x.
- Zhou, B., Sherriff, B.L., Wang, T., 2009. 27Al NMR spectroscopy at multiple magnetic fields and ab initio quantum modeling for kaolinite, 94, pp. 865–871. https://doi. org/10.2138/am.2009.3142.